International Journal of Applied Earth Observation and Geoinformation 50 (2016) 159–169

Contents lists available at ScienceDirect

International Journal of Applied Earth Observation and Geoinformation

journal homepage: www.elsevier.com/locate/jag

Determining surface magnetic susceptibility of loess-paleosol sections based on spectral features: Application to a UHD 185 hyperspectral image

Jing Cui [a,b], Shimin Zhang [a,*], Jingfa Zhang [a], Xudong Liu [a], Rui Ding [a], Hanyong Liu [a]

[a] Key Laboratory of Crustal Dynamics, Institute of Crustal Dynamics, China Earthquake Administration, Beijing 100085, China
[b] China University of Geosciences (Beijing), Beijing 100083, China

ARTICLE INFO

Article history:
Received 3 August 2015
Received in revised form 22 March 2016
Accepted 30 March 2016

Keywords:
Hyperspectral
Magnetic susceptibility
UHD 185

ABSTRACT

Magnetic susceptibility (MS) records of loess-paleosol sequences have been considered a measure of the degree of pedogenic activity and are considered to be excellent proxies for terrestrial climatic fluctuations. However, the MS of single (vertical) path variations occasionally represents site-specific influences rather than monsoonal changes (depending on the position of the path). Few studies have used remote sensing techniques to map the surface MS information of loess-paleosol sections. Hyperspectral techniques provide an efficient, economical and quantitative alternative. In this study, stepwise regression was used to build MS estimation models based on spectral features. Six MS models based on spectral features were established. Test datasets indicated that our models are very successful, all resulting in $R^2 > 0.92$ and RMSEs ranging from 4.5736 to 6.80475. The slope change between 810 nm and 880 nm (b880/b810) observed in all models played an important role in MS estimation. Models 5 and 6 have higher RMSEs and relatively lower SAM values, although the R^2 values are both above 0.95. The RMSEs of the first four models are similar. Therefore, the first four models were thought to be more stable and useful.

UHD 185, a new generation of commercial hyperspectral imaging sensor, was used for surface MS mapping of a loess-paleosol section by model 1 and model 2. The MS map corresponded well to the loess sequences. The MS values obtained from the UHD 185 data are convincing and consistent with the measured data ($R^2 > 0.85$). The trend in changing MS values is clear, suggesting that model 1 and model 2 could produce reasonable loess-paleosol section surface maps from the UHD 185 image, although there is a linear offset between the estimated MS and the measured MS. The methodology proposed here can be used to map MS on a much larger scale. Because of the limit of the spectral range, the performances of model 3 and model 4 with the image were not discussed. However, they have been shown to be successful according to the laboratory test data.

1. Introduction

Magnetic susceptibility (MS) records of loess-paleosol sequences have been studied in the past and are considered to be an effective measure of the degree of pedogenic activity and excellent proxies for terrestrial climatic fluctuations (Liu, 1985; An et al., 1991; Verosub et al., 1993; Heller and Liu, 1982, 1984, 1986; Heller and Evans, 1995; Porter et al., 2001; Kohfeld and Harrison, 2003; Maher et al., 2003; Stevens and Lu, 2009; Smith et al., 2011). Usually, low susceptibility implies periods in which the summer monsoon was weak and cold, with reduced pedogenic activity. Conversely, high susceptibility values usually imply periods when the summer monsoon was warm and moist, with strong pedogenic activity (An et al., 1991). MS is an important physical parameter of soils and sediments (Tompson and Oldfield, 1986; Heller and Evans, 1995; Jin et al., 2003). Traditional methods to generate a susceptibility profile for a several-meter-thick sediment section would take an hour or more, while MS profiles are commonly taken along a single (vertical) path. However, typically, the internal consistency of the vertical line MS data is not tested by replicating values along other parallel profiles (Porter et al., 2001).

* Corresponding author at: Institute of Crustal Dynamics, CEA, 1 Anningzhuang Road, Haidian District, Beijing 100085, China.
E-mail addresses: jingcui_86@yahoo.com, cuijing99@163.com (J. Cui), zhangshimin@263.net (S. Zhang).

http://dx.doi.org/10.1016/j.jag.2016.03.016
0303-2434/

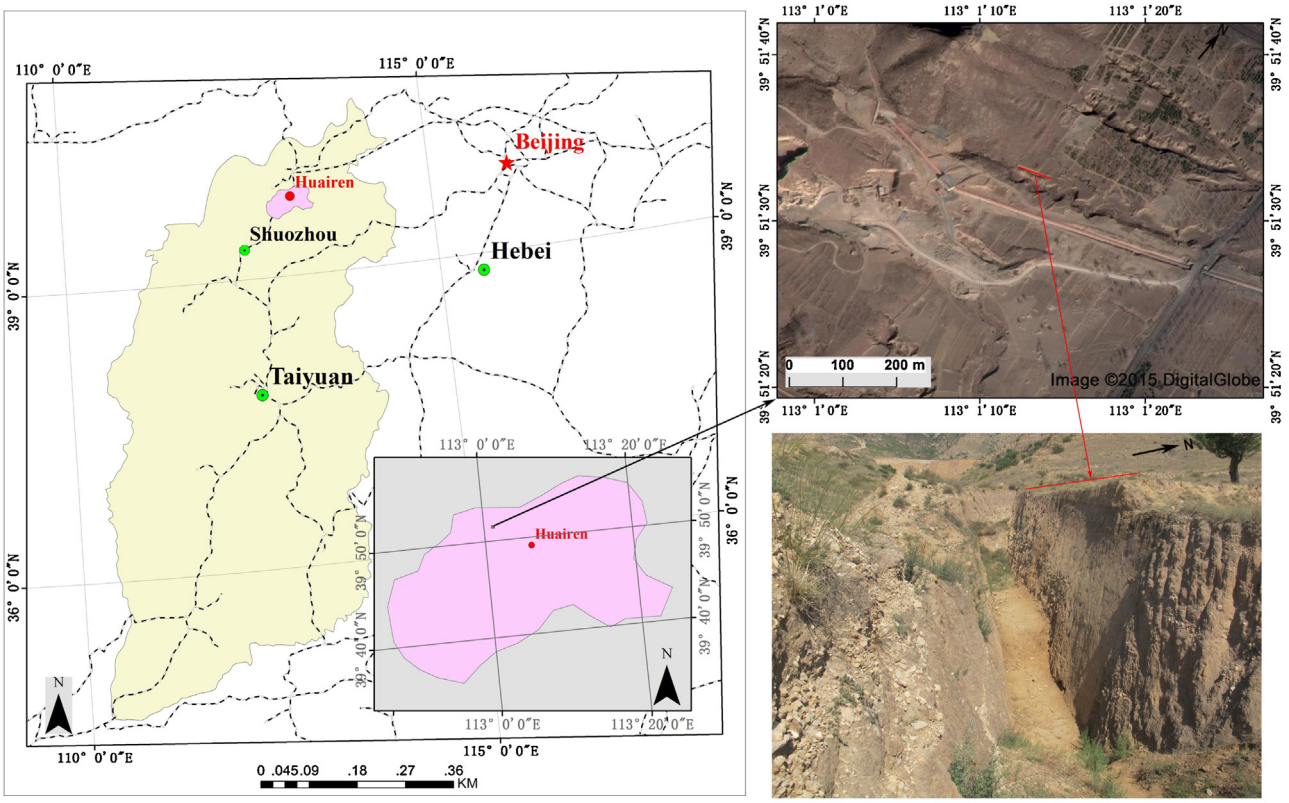

Fig. 1. Location of the study area.

Image source: Digital Globe

The image of the loess-paleosol section could enlarge the datasets covering variation over a wide vertical and lateral range. Grayscale intensity and whiteness data for sections in a range of climatic and latitudinal settings display a high degree of correlation with magnetic susceptibility data (Porter et al., 2001; Chen et al., 2002). Indeed, Ji et al. (2004a,b) first used TM images to estimate the MS of surface soil on the Loess Plateau at a large scale, obtaining good results. Previous laboratory studies focused on correlations between reflectance spectroscopy and MS show the potential of MS mapping with hyperspectral images (Jin et al., 2003; Smith et al., 2011). These works are all based on the premise that reflectance is related to the composition and structure of constituent minerals. However, few studies have used remote sensing techniques to map the surface MS information of loess-paleosol sections, which is useful for rapidly characterizing multiple loess sequences and linking the stratigraphic changes to monsoonal processes (Smith et al., 2011). Further, local and post-depositional effects can cause variation in the response of magnetic susceptibility. Smith et al. (2011) obtained an image of a loess-paleosol profile using a Nikon D80 and first processed the image to a single RGB and NIR file. Their work suggests that the bands used by cameras are too broad for MS estimation.

Hyperspectral remote sensing refers to the use of a very narrow, continuous spectrum of remote sensing image that features continuous channel technology. The abundant spectral information of the hyperspectral image could provide the ability to establish a link between reflectance and MS. The objectives of this study are to define a new model based on spectral features to mapping MS of a loess-paleosol section and to apply this model to a sensor with limited spectral range to see how well it performs.

2. Materials and methods

We aimed to determine the correlation between magnetic susceptibility and reflectance spectra. This required understanding the spectral features of the soils and then choosing those parameters that correlated with MS, allowing us to construct a model for MS estimation.

2.1. Site description and sample collection

The Emaokou section is located to the northwest of the town of Huairen, in Shanxi Province (Fig. 1), centered at longitude 113° 1′ 13.10″E and latitude 39° 51′ 33.04″N. The main landforms in the study area are loess platforms. The cross section shown in Fig. 2 includes Malan Loess (L_1), the Holocene Black Loam paleosol (S_0), a distinct loess layer (L_0) and a gravel layer. For this study, we sampled only the loess-paleosol sequence (between the two dashed yellow lines in Fig. 2), excluding the bottom gravel layer and the top loess layer (L_0). We collected samples from S_0 and L_1 along model line 1, model line 2 and the test line for laboratory analysis (model line 1, 2 and the test line are shown in Fig. 2). The sampling interval was 10 cm from the top to the bottom. Samples from model line 1 (37 samples) and model line 2 (35 samples) were used to build the model. Samples from the test line (55 samples) were used for model testing.

2.2. Magnetic susceptibility measurement

The low-frequency magnetic susceptibility of the samples was measured at 976 Hz using a MFK1-FA Multi-Function Kappabridge magnetic susceptibility meter (Pokorny et al., 2006), a product of the Advanced Geoscience Instruments Company (AGICO) of the

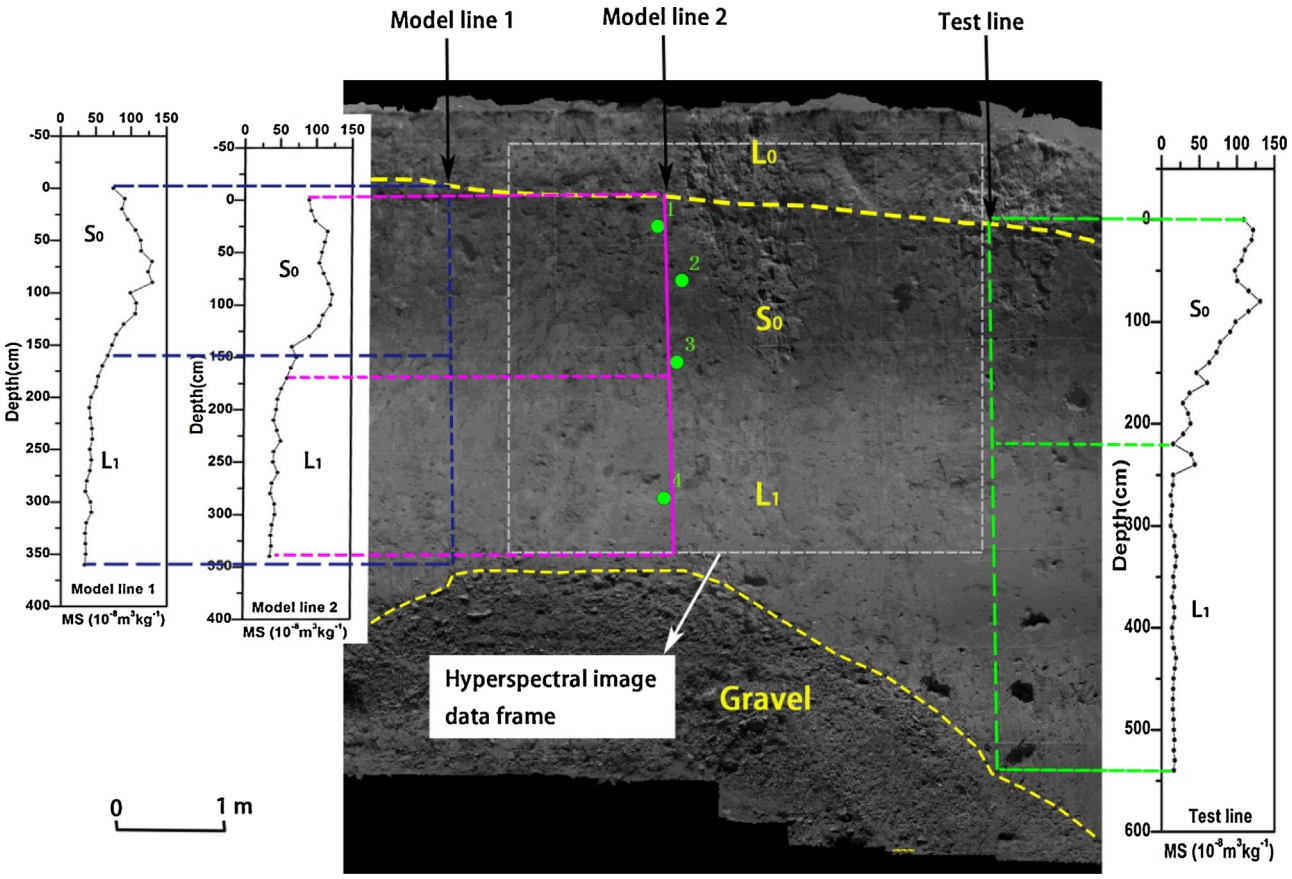

Fig. 2. Photograph of the studied section with the profiles labeled. The points were used for hyperspectral reflectance assessment.(For interpretation of the references to colour in the text, the reader is referred to the web version of this article.)

United States. This instrument can measure magnetic susceptibility at three operating frequencies: 976, 3904 and 15,616 Hz. In this study, we used the low-frequency magnetic susceptibility presented as mass susceptibility. Xu's work showed that loess-paleosol samples could be detected at a low frequency (976 Hz) (Xu et al., 2012). The SI unit of mass susceptibility is $m^3\ kg^{-1}$.

2.3. Hyperspectral image acquisition

Hyperspectral image data were collected using a UHD 185 sensor from the Cubert GmbH Company, the data acquisition sketches of which are shown in Fig. 3. The Cubert UHD 185 sensor was fitted with fiber optics with a 27° field of view and operated in the 450–950 nm spectral region at a sampling interval of 4 nm, with 125 channels. The spectral throughput is 2500 spectra for one cube. Surface measurements were conducted on May 20, 2015, under cloudless conditions between 10:30 and 14:30. Measurements were taken at a distance of 9 m from the vertically oriented loess surface, and hyperspectral images were acquired at a spatial resolution of 4.22 cm. The image was sampled to 5 cm × 5 cm for one pixel. Reference measurements on a white board were made prior to each measurement, with the board oriented vertically to better represent the loess surface. We used Spectralon as the whiteboard, which is manufactured from a sintered polytetrafluoroethylene-based material (PTFE). Then, the dark current measurements were made. Dark measurements were taken by placing the black plastic lens cap over the lens so that no light could pass through. This solution is ideal for non-laboratory environments. To obtain reflectance measurements, the dark measurement was subtracted from the actual measured values and the reference values and then divided by this reference. This common technique guarantees clean and accurate results. The average calculation of the dark image is highly recommended to have stable values by not subtracting some momentary high noise peaks, which do not exist in the other measurements.

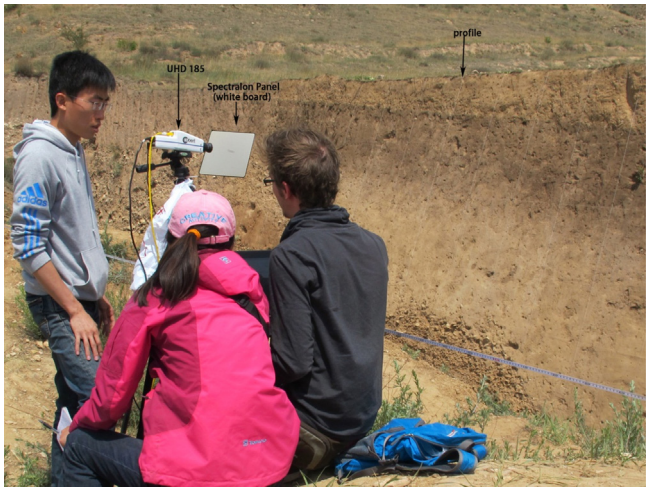

Fig. 3. Overview of equipment setup.

2.4. Reflectance measurement

The reflectance spectra of the samples were measured using an ASD Field Spec 3 spectrometer (Analytical Spectral Devices,

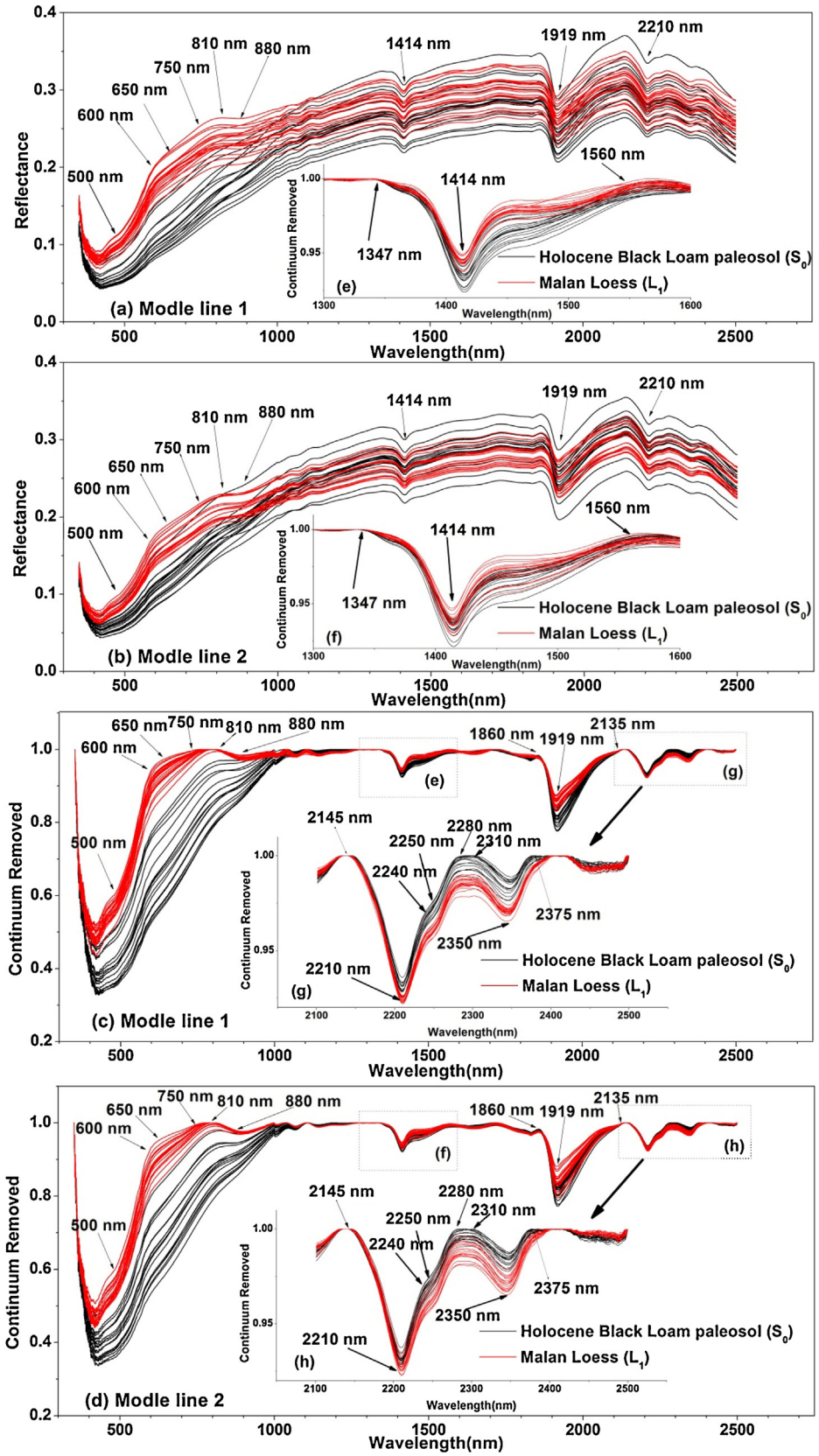

Fig. 4. Sample reflectance and continuum-removed spectra.(For interpretation of the references to colour in the text, the reader is referred to the web version of this article.)

Boulder, USA, produced in 2008). We analyzed samples in the 350–2500 nm spectral region at sampling intervals of 1 nm. An ASD contact probe attachment with an integral illumination source was used, and the samples were rotated by approximately 90°. For measurements, the contact probe was kept stationary, and an average of 30 consecutively acquired spectra were recorded to reduce the

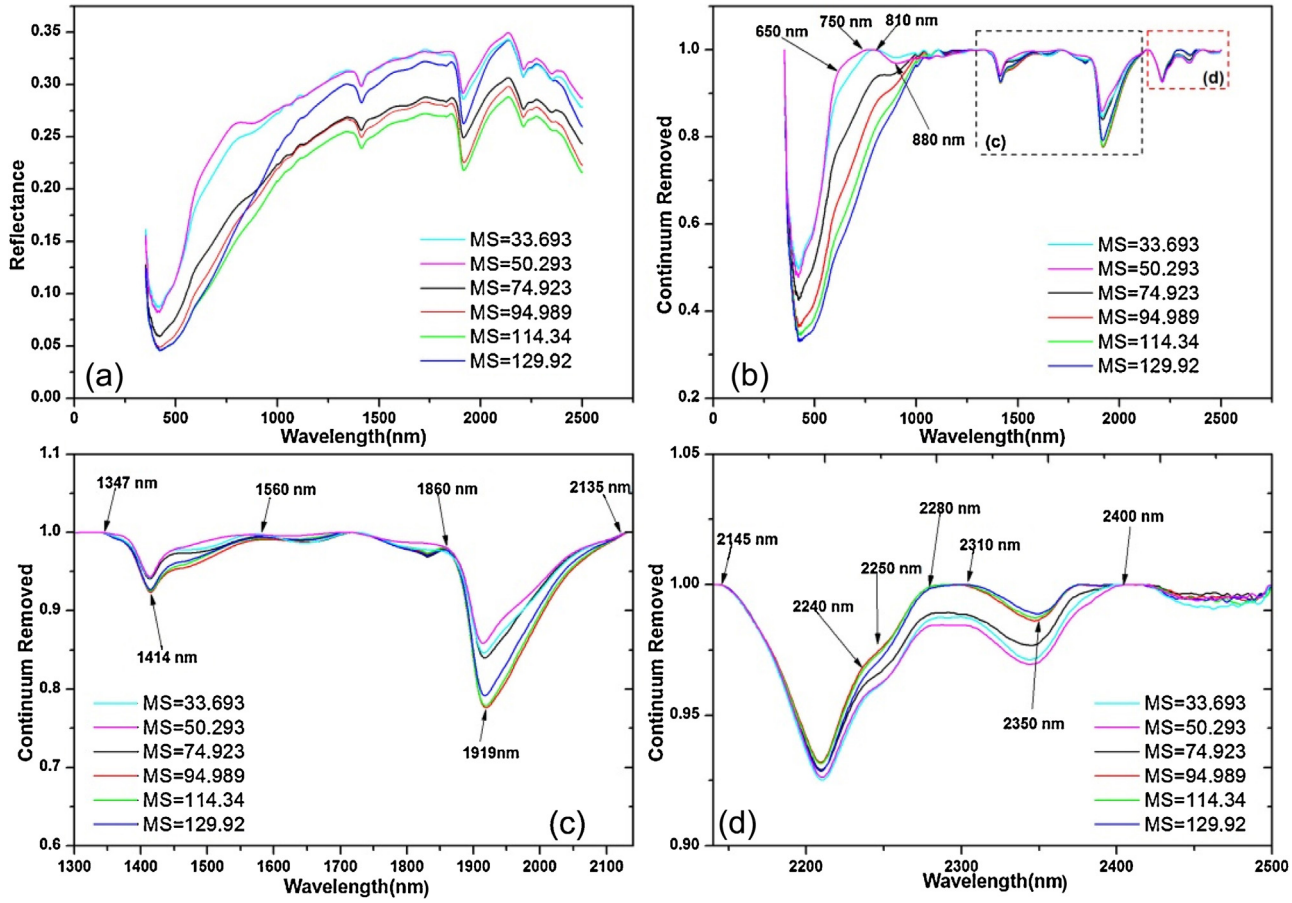

Fig. 5. Spectral features of samples versus their MS values.

noise level. For measurement of the field reflectance spectra, we first ensured that the surface was uniform and that the area was greater than or equal to 5 cm × 5 cm. Surface reflectance measurements were taken at five sites within each point. The average of the five measurements was used as the reflectance of the point. For the laboratory reflectance spectroscopy measurements, the samples were ground to <0.6mm with a mortar (30 mesh) to reduce the effect of grain size variations on sample brightness. All reflectance spectra were post-processed using the ViewSpec^{TM} Pro 6.0 software (ASD Inc, 2008), mainly in the form of spectral averaging and splice correction. For the splice correction, a bias value was calculated for the VNIR and SWIR2 regions, which are offset to match the SWIR 1 regions at the splice point. This is usually performed only for presentations and documentation or when using data to match against a spectral library rather than to correct the data (ASD Inc, 2008). In total, four field points were measured for image calibration (green in Fig. 2), 72 samples (from model line 1 and model line 2, described in chapter 2.1) were measured in the laboratory for modeling, and 55 samples (from test line, described in chapter 2.1) were measured in the laboratory to verify the modeling results.

2.5. Continuum removal

A continuum removal (CR) process was used for spectral feature analysis. The CR process isolates spectral features and allows them to be compared more efficiently. CR was applied to the sample spectra to reduce the effect of optical constants and to highlight each spectrum's absorption features for ease of comparison (Clark, 1999). Scattering and Beer's Law make the effects non-linearly multiplicative (Clark and Roush, 1984). Thus, the continuum should be removed by division. In this study, the continuum is removed by dividing the reflectance value for each point in the absorption feature by the reflectance level of the continuum line at the corresponding wavelength (Zhi et al., 2004).

2.6. Linear regression

Linear regression estimates the coefficients of the linear equation, involving one or more independent variables that best predict the value of the dependent variable. Stepwise regression was used to determine the relationship between MS and spectral features (Smith et al., 2011). Stepwise is one of the linear regression variable selection methods. At each step, the independent variable not in the equation that has the smallest probability of F is entered if that probability is sufficiently small. Variables already in the regression equation are removed if their probability of F becomes sufficiently large. The method terminates when no more variables are eligible for inclusion or removal (IBM SPSS, 2010), where F means the F statistics (Furundzic, 1998). Following the stepwise regression procedure, the regression model could be defined. The model was then applied to the spectra for the testing data set to estimate the MS value. The accuracy of this estimation was reported both in terms of the coefficient of determination (R^2) between estimated and measured MS values and the root mean square error (RMSE) of these estimations. In this study, some parameters based on the spectral features were used as independent variables, while the measured MS values were used as dependent variables in the stepwise regression. IBM SPSS statistics Base 19 software was used for stepwise regression, and the probability of F was used as the stepping method criteria (IBM SPSS, 2010). For the stepping method criteria, a

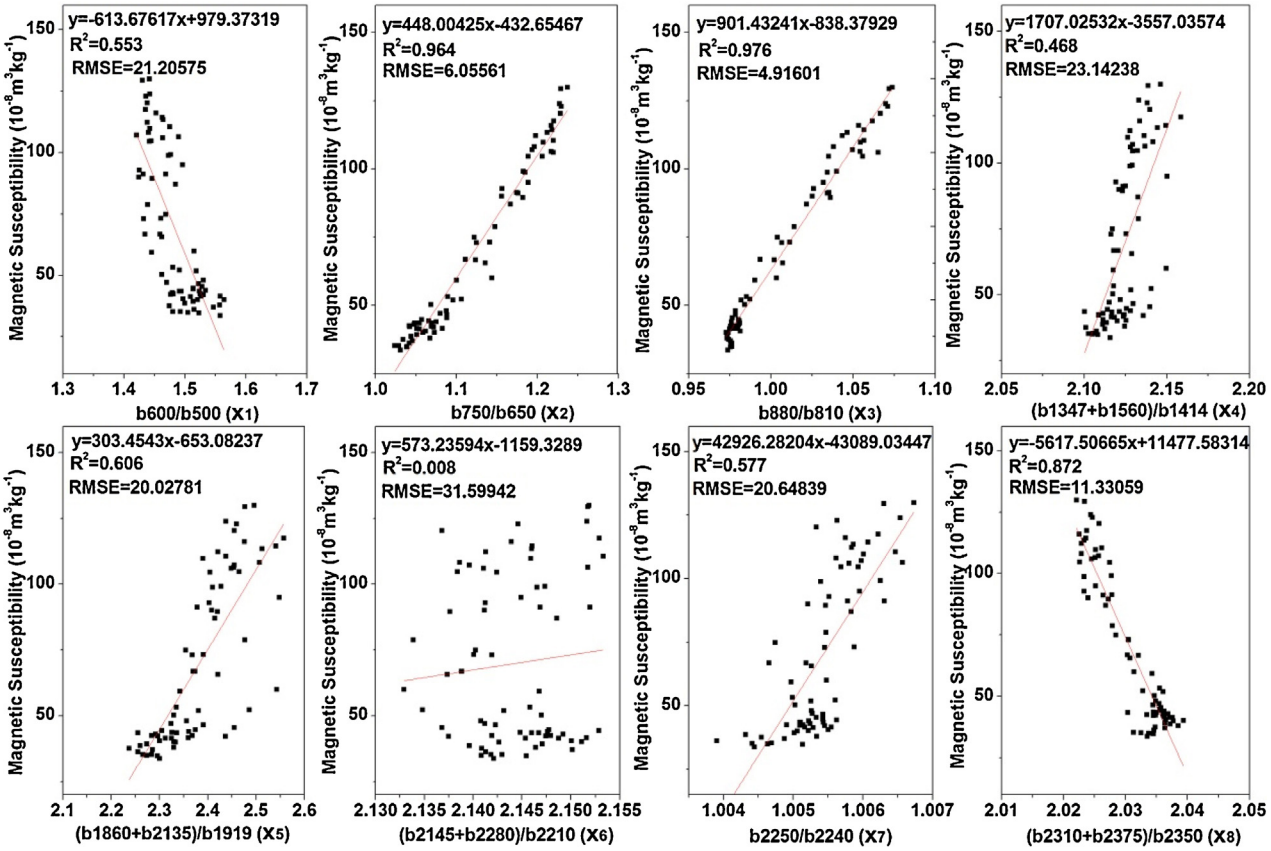

Fig. 6. Linear regression between band ratios and MS.

variable is entered into the model if the significance level of its F value is less than 0.05 and is removed if the significance level is greater than the 0.1 (IBM SPSS, 2010; Furundzic, 1998; Smith et al., 2011).

2.7. Spectral analysis

In this study, the spectral analyst tools of the ENVI 5.1 classic software was used for assessment of the MS estimation model and the image spectra. For spectral analysis ENVI's Spectral Analyst was used to assist with mineral identification with the image spectra being compared to that extract from ASD. This tool uses processes such as Binary Encoding, Spectral Angle Mapper, and Spectral Feature Fitting to rank the match of an unknown spectrum to the material in a spectral library. In this case Spectral Angle Mapper was used because Spectral Feature Fitting is suitable for wavelength range of specific absorption feature rather than whole spectral shape and Binary Encoding has lower match accuracy than Spectral Angle Mapper. The measurements of MS and soil spectral were used as the input spectral library.

3. Results and discussion

3.1. Characterization of the spectra

The spectra of field samples from model line 1 and model line 2 are shown in Fig. 4 (model lines 1 and 2 are described in Section 2.1). The black dashed line indicates spectra from S_0, and the red solid line indicates spectra from L_1. Fig. 4 (a–b) shows the original spectra of these samples while Fig. 4(c–f) shows the continuum-removed spectra of these samples. Six absorption features are found near 450 nm, 900 nm, 1414 nm, 1919 nm, 2210 nm and 2350 nm (Fig. 4). There is a subtle shoulder at 2250 nm between 2210 nm and 2280 nm. The absorption features near 500 and 900 nm are typical of Fe^{3+} and Fe^{2+} (Deaton and Balsam, 1991; Palacios-Orueta and Ustion, 1998; Clark, 1999). Narrow absorption features close to 1414 nm and 1919 nm indicate the occurrence of water bound in the interlayer lattices (Bishop et al., 1994). An absorption peak centered at 2210 nm is typical of Al-OH minerals, such as illite and muscovite, whereas Mg-OH minerals have absorption features at 2250 and 2350 nm (e.g., epidote and chlorite). Finally, carbonate minerals such as calcite have an absorption feature at 2355 nm (Clark, 1999; Cui et al., 2014; Smith et al., 2011).

The spectra of S_0 and L_1 differ from 500 to 900 nm and from 2150 to 2350 nm. Four slope changes and two absorption depths classify the two soil types (Fig. 4). These slope changes occur between 500 and 600 nm, between 650 and 750 nm, between 800 and 900 nm and between 2240 and 2250 nm with absorption depths of 2210 nm and 2350 nm. Thus, from an empirical perspective, these regions offer possible explanatory power as ratios. The band ratio has been shown to have a close correlation with MS (Smith et al., 2011). Thus, band ratio analysis was used to represent the slope change and the absorption features. Specific bands were chosen depending on spectral transition (shown in Fig. 4) and personal experience. For example, the slope change between 500 and 600 nm was replaced by b600/b500, where the b600 indicates a reflectance value at 600 nm, which is the same as the other parameters (i.e. b500, b2210, etc.). The absorption depth at 2210 nm was replaced by (b2145 + b2280)/b2210, where b2145 and b2280 indicate the shoulder is near b2210. Thus, the four slope changes were shown as b600/b500, b750/b650, b880/b810 and b2250/b2240. The two absorption depth features were shown as (b2145 + b2280)/b2210 and (b2310 + b2375)/b2350. Additionally, the absorption features close

Table 1
Regression analysis results for the combination of bands.

Model	Band combination	Regression equation	R^2	RMSE
Model 1	x_3	$y = 901.43241x_3 - 838.7929$	0.976	4.66195
Model 2	x_2, x_3	$y = 156.031x_2 + 611.195x_3 - 720.95778$	0.984	3.87509
Model 3	x_2, x_3, x_8	$y = 167.425x_2 + 451.607x_3 - 944.318x_8 + 1344.654$	0.989	3.25924
Model 4	x_1, x_2, x_3, x_8	$y = -44.063x_1 + 182.938x_2 + 409.996x_3 - 725.959x_8 + 991.077$	0.990	3.14034
Model 5	x_1, x_2, x_3, x_6, x_8	$y = -57.052x_1 + 215.623x_2 + 311.006x_3 + 263.395x_6 - 886.621x_8 + 835.006$	0.991	1.97576
Model 6	x_1, x_2, x_3, x_6, x_7, x_8	$y = -68.190x_1 + 270.756x_2 + 234.731x_3 + 411.008x_6 - 3336.674x_7 - 823.919x_8 + 3777.453$	0.992	2.87888

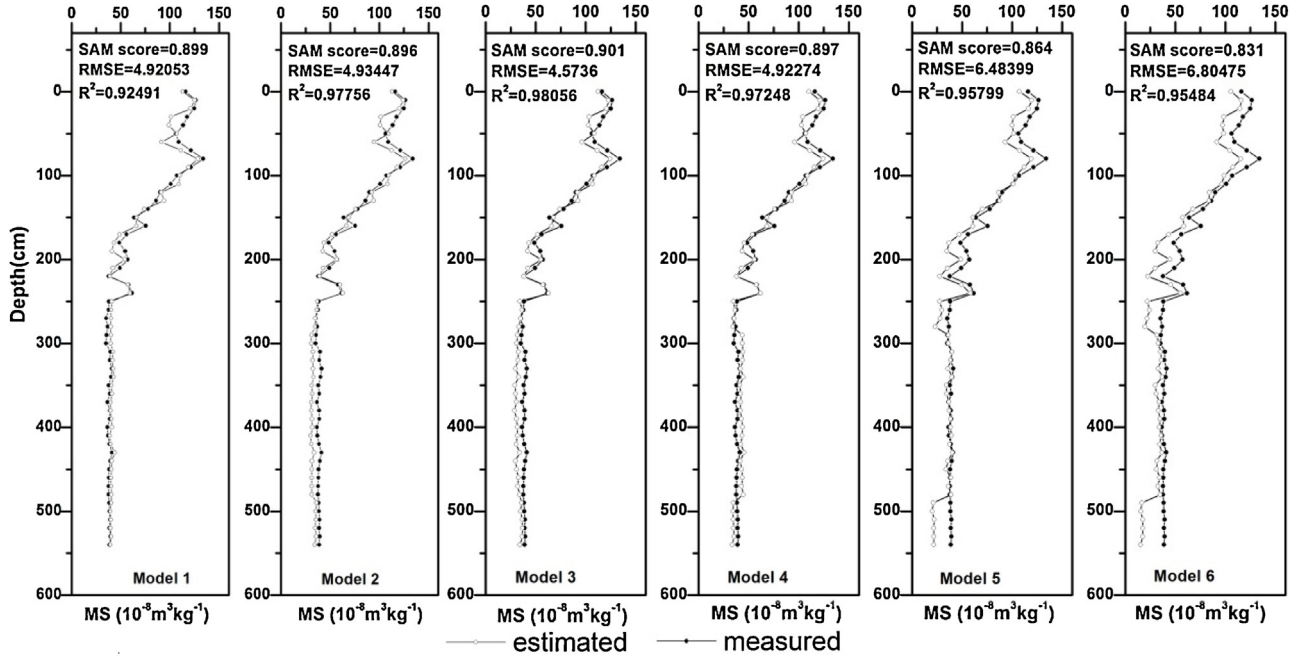

Fig. 7. Comparison of the instrumentally measured and spectrally estimated MS of the test data.

to 1414 nm and 1919 nm were shown as (b1347 + b1560)/b1414 and (b1860 + b2135)/b1919. For ease of expression, b600/b500, b750/b650, b880/b810, (b1347 + b1560)/b1414, (b1860 + b2135)/b1919, (b2145 + b2280)/b2210, b2250/b2240 and (b2310 + b2375)/b2350 were named x_1, x_2, x_3, x_4, x_5, x_6, x_7 and x_8, respectively. Fig. 2 shows the two soil types corresponding to the different MS values. We want to determine the relationship between these spectral features and MS.

Fig. 5 shows the reflectance spectra of samples with different MS values. It shows that the x_1 and x_8 values gradually decrease as the MS value increases. In contrast, x_2 and x_3 gradually increase as the MS value increases. There was no regular change in x_4, x_5, x_6 and x_7 with an increase in MS values. The scatter plots (Fig. 6) for the band ratios (x_1, x_2, x_3, x_4, x_5, x_6, x_7 and x_8) against MS further confirm that x_2, x_3 and x_8 show a strong linear relationship with MS, with R^2 values all above 0.85 (Fig. 6).

3.2. Model construction

Our objective is to develop regression models for MS estimation based on the spectral features. The above analysis indicated that some band ratios have a close correlation with MS (Fig. 6). However, we still want to understand which of the above eight band ratios should be included in a regression model. As a result, a stepwise regression was used for the model construction in this study. The stepwise regression has been described in chapter 2.6. The above eight parameters (x_1, x_2, x_3, x_4, x_5, x_6, x_7 and x_8) were used as independent variables, and the measured MS values were used as dependent variables in the stepwise regression. After the stepwise regression procedure, six regression models were obtained (Table 1). The R^2 values of the six models are all above 0.97, and x_3 was present in all six models. This suggests that x_3 plays an important role in MS estimation. In addition, x_2 also plays an important

Table 2
XRD results of sample.

Samples	Compositions
1 (L_1)	Quartz(34%) + Albite(27%) + Microcline(12%) + Calcite(12%) + Chlorite(5%) + Muscovite(3%) + Amphibole(3%) + Dolomite(3%)
2 (L_1)	Quartz(38%) + Albite(22%) + Microcline(10%) + Calcite(13%) + Clinochlore(5%) + Muscovite(3) + Amphibole(3%) + Dolomite(3%)
3 (L_1)	Quartz(35%) + Albite(25%) + Microcline(9%) + Calcite(14%) + Clinochlore(4%) + Muscovite(2%) + Amphibole(1%) + Dolomite(10%)
4 (L_1)	Quartz(44%) + Albite(19%) + Microcline(10%) + Calcite(14%) + Clinochlore(5%) + Muscovite(3%) + Amphibole(4%)
5 (S_0)	Quartz(42%) + Albite(26%) + Microcline(7%) + Calcite(9%) + Clinochlore(5%) + Muscovite(2%) + Dolomite(8%) + Hematite(1%)
6 (S_0)	Quartz(49%) + Albite(27%) + Microcline(5%) + Calcite(6%) + Clinochlore(5%) + Muscovite(3%) + Amphibole(3%)+ Hematite(1%)
7 (S_0)	Quartz(45%) + Albite(29%) + Microcline(10%) + Calcite(8%) + Clinochlore(4%) + Muscovite(3%) + Amphibole(1%)+ Hematite(1%)
8 (S_0)	Quartz(50%) + Albite(24%) + Microcline(7%) + Calcite(10%) + Clinochlore(4%) + Muscovite(2%)+ Hematite(2%)

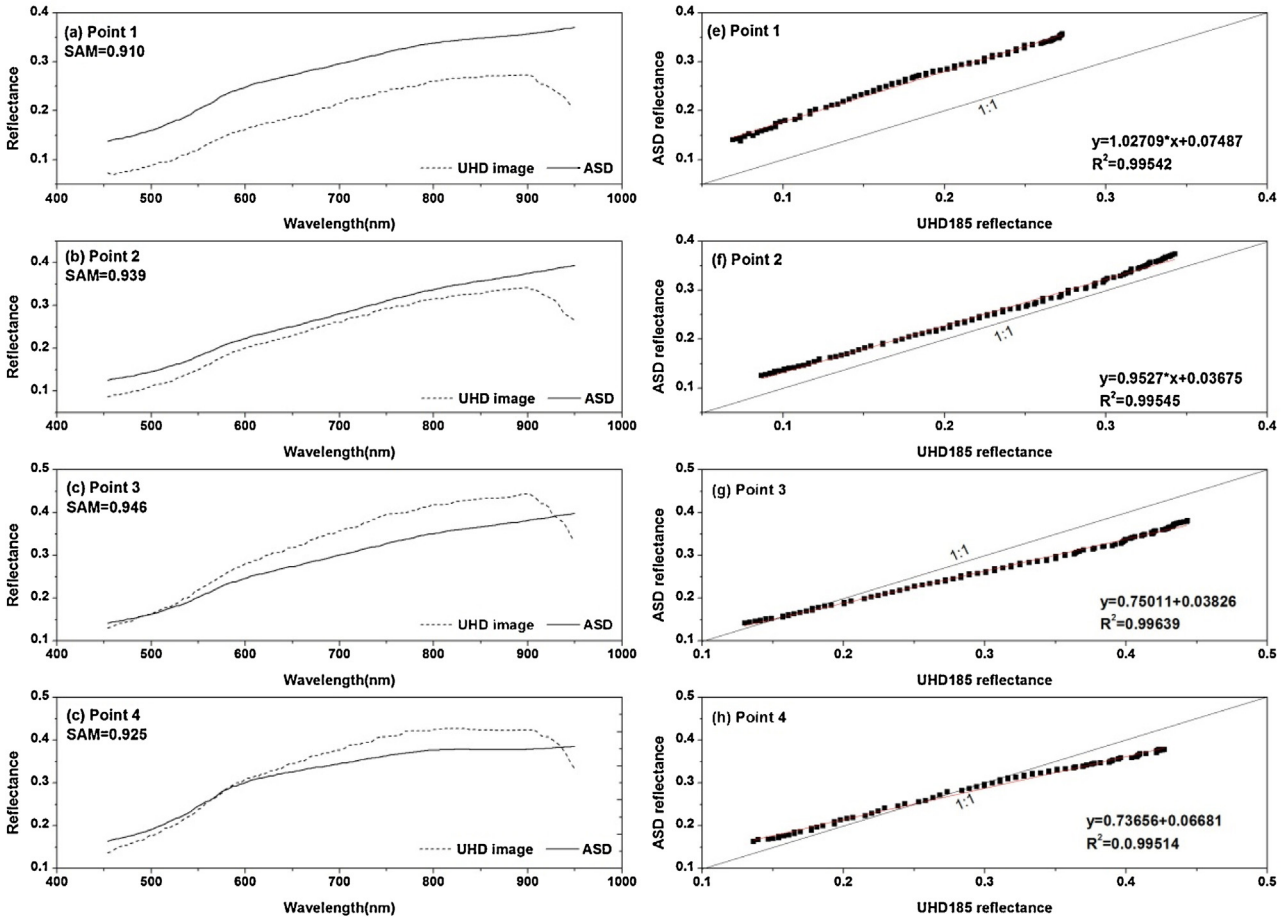

Fig. 8. Reflectance spectra from the UHD 185 image and field reflectance spectra.

role and is present in five models. One explanation for this outcome could be that absorption of these wavelengths by the samples may be influenced by Fe^{3+} and Fe^{2+}. Hematite and geotite have spectral features near 650 nm and 880 nm. X-ray diffraction (XRD) analyses were conducted for eight samples from the section. Four samples were from S_0, and four samples were from L_1. The XRD results (Table 2) indicate that hematite was the dominant iron oxide contained in S_0. Previous work has shown that hematite exhibits a positive correlation with MS (Ji et al., 2001). However, we cannot conclude that hematite is the only dominant mineral control of MS in these sample soils. Indeed, the real world (and, for that matter, the universe) is a complex mixture of materials at almost any scale. Diffuse reflectance spectrophotometry has a detection limit for iron oxides that is at least an order of magnitude lower than XRD (Deaton and Balsam, 1991). Additionally, fine-grained citrate-bicarbonate-dithionite-extractable iron oxide minerals are the dominant factor controlling reflectance changes and MS of loess and paleosol samples (Ji et al., 2004b). Therefore, changes in x_2 and x_3 could be the result of a concentration of various magnetic minerals.

Models 3–6 contain the parameters x_6-x_8. Illite/muscovite and montmorillonite both have excellent potential utility as weathering indicators (Smith et al., 2011). Calcite is the dominant carbonate mineral in the loess (Table 2), as it is susceptible to weathering and leaching. Weathering would deplete some of the iron oxides and hence would influence the MS. However, the model accuracy was not improved significantly by adding these parameters (x_6–x_8). This indicates that x_6-x_8 are not the dominant factors controlling MS of the loess and paleosol samples.

We found that x_4 and x_5 are absent in the six models. One explanation for this finding could be that the absorption of these wavelengths by the samples may be influenced by water content. Absorption at 1400 nm is related to the first overtone of the O—H stretching modes associated with water or hydrous minerals (Clark et al., 1990; Viscarra Rossel and Chen, 2011). The difference between these causes a slight displacement of the peak, which can be very difficult to distinguish within the soil spectra. The 1900 nm wavelength is a combination band involving the stretching and bending modes of the H_2O molecule and is thus specific of molecular water (Clark et al., 1990). Galva˜o et al. (2001) also excluded these two wavelengths in their study of the reflectance of tropical soils.

The above six models were applied to the testing data (55 samples) to estimate the MS (Fig. 7). SAM scores of the estimated MS curve and measured MS curve are all above 0.8, indicating a close match in terms of shape. There is a strong correlation (R^2 above 0.92, RMSE ranging from 4.5736-6.80475) between the estimated and measured MS data of the soil samples. Models 5 and 6 have higher RMSEs and relatively lower SAM values, although the R^2 is above 0.95. The RMSE values of the first four models are similar, suggesting that the first four models are more stable. The first four models are capable of MS estimation.

3.3. Assessment of the image spectra

The spectral range of the UHD 185 image is 450–950 nm, so models 1 and 2 in Table 1 can be used for application. We need to assess the accuracy of the image spectra data before applying our model

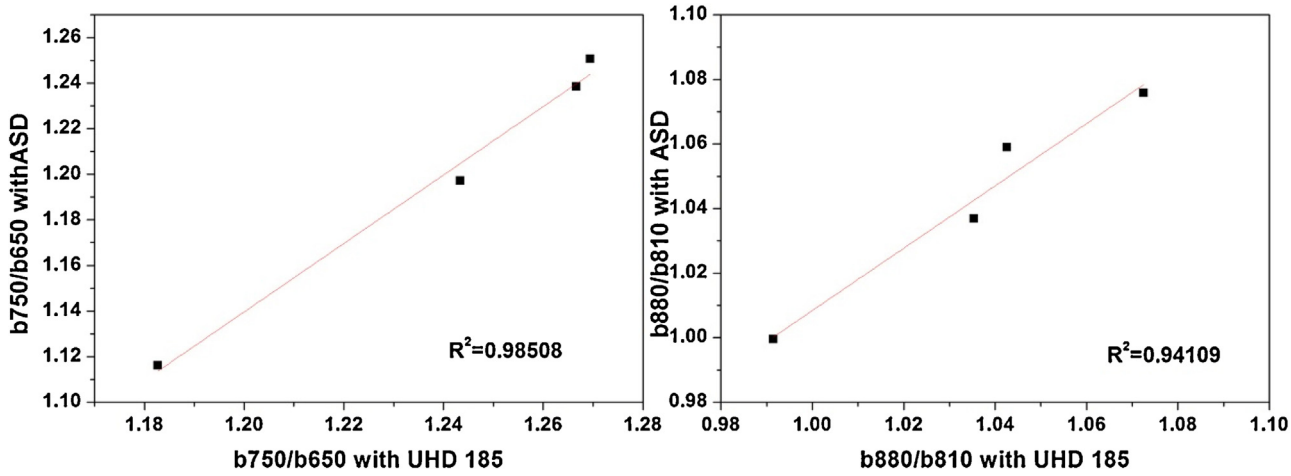

Fig. 9. Band ratio comparison of UHD 185 and field measurements.

to the hyperspectral image. The spectra from the UHD 185 image compared favorably with the field spectral measurements, except for the range of 900–950 nm (Fig. 8). The reflectance in the range of 900–950 nm markedly declines, which is not consistent with the real soil spectral shape (Figs. 4 and 8). The SAM scores are all greater than 0.90 (except in the range of 900–950 nm), indicating a good match between the spectral shape of the image and the field spectra (except in the range of 900–950 nm). The R^2 values between UHD 185 reflectance and ASD reflectance are all above 0.995.

To further assess the above results, we used band ratios of b750/b550 and b880/b810 to quantify relative variations in the spectral shape of the UHD 185 reflectance data. The two band ratios were evaluated because their combination was used for estimating the MS (models 1 and 2 in Table 1). The band ratios of b750/b550 and b880/b810 with UHD 185 reflectance display a strong correlation with the band ratios of b750/b550 and b880/b810 with ASD measured reflectance ($R^2 = 0.98508$ and $R^2 = 0.94109$, respectively; Fig. 9).

The average ratio difference and percentage of the mean can be calculated using the following equations:

$$\overline{Diff.ratio} = \sum_{n=1}^{N} \frac{UHD185_n(bi/bj) - ASDn(bi/bj)}{N},$$

$$Percentage = \frac{\overline{Diff.ratio}}{ASDn(bi/bj)} \times 100\%$$

where n is the point number and i and j are the wavelengths of UHD 185. $\overline{Diff.ratio}$ is the average ratio difference, bi/bj is compiled from the wavelength i and wavelength j reflectance, $UHD185_n(bi/bj)$ is the UHD 185 band ratio and $ASDn(bi/bj)$ is the average of the UHD 185-resampled ASD measured band ratio. The average band ratio differences of b750/b550 and b880/b810 were calculated to be 0.059745 and −0.00718 (i.e., 5.059% and −0.6%), respectively.

3.4. Application to a hyperspectral image

After the assessment of the UHD 185 image data, we applied models 1 and 2 to the UHD image (Fig. 10). The image can be classified into three parts by color; the upper layer (green, Fig. 10(c–d)) corresponds to the distinct loess layer (L_0), the middle layer (red, Fig. 10(c–d)) corresponds to the Holocene Black Loam paleosol (S_0), and the bottom layer (green, Fig. 10(c–d)) corresponds to the Malan Loess (L_1). Because there is a small plant in the right upper-middle image, we mask this area, which is shown as a white patch in Fig. 10(c–d). The boundary of the S_0 and L_1 is more easily identified with the naked eye by the MS map than with the photograph. The MS map corresponds well to the loess sequences, indicating that monsoonal processes influence the stratigraphic changes in the study area (An et al., 1991). Low susceptibility implies periods in which the summer monsoon was weak and cold, while high susceptibility values imply periods when the summer monsoon was warm and moist (An et al., 1991). The MS map also indicates that using a single (vertical) path to measure the MS has some limitations, as local and post-depositional effects can cause variation in the response of magnetic susceptibility. The MS of single (vertical) path variations sometimes represents site-specific influences rather than monsoonal changes (depending on the position of the path). For example, the MS distribution in rectangle A is different from that of rectangle B (Fig. 10(c–d)). MS profiles taken along a single (vertical) path in rectangle A and rectangle B would yield different results.

To evaluate the accuracy of the surface MS distribution map, the vertical MS values of model line 2 (35 samples, described as Section 2.1) were selected for testing. The lines of estimated MS values and measured MS values were consistent in shape (Fig. 10(b)). There is a linear relationship between the measured MS and the estimated MS ($R^2 > 0.85$, Fig. 11). The trend in changing MS values is clear, which suggests that models 1 and 2 could reasonably produce loess-paleosol section surface maps from the UHD 185 image, although there is a linear offset between the estimated and measured MS, and there is a tendency towards overestimation of MS values. This offset requires further study.

4. Conclusions

The results of our study demonstrate that absorption features of the reflectance spectra can successfully estimate the MS of loess-paleosol sections. Six MS models based on spectral features were established. x_3 (b880/b810) was present in all models, indicating that it plays an important role in MS estimation. x_6, x_7 and x_8, which correspond to illite, muscovite, montmorillonite and carbonate minerals related to weathering, have an influence on the MS. However, the model accuracy was not improved significantly when x_6-x_8 were added. This indicates that x_6–x_8 are not the dominant factors controlling the MS of the loess and paleosol samples. Test datasets indicated that our models are very successful, with all models yielding $R^2 > 0.92$ and RMSE in the range of 4.5736–6.80475. Models 5 and 6 have higher RMSEs and relatively lower SAM values, although the R^2 values are both above 0.95. The RMSE values of the first four models are similar, suggesting that these models are more stable and useful.

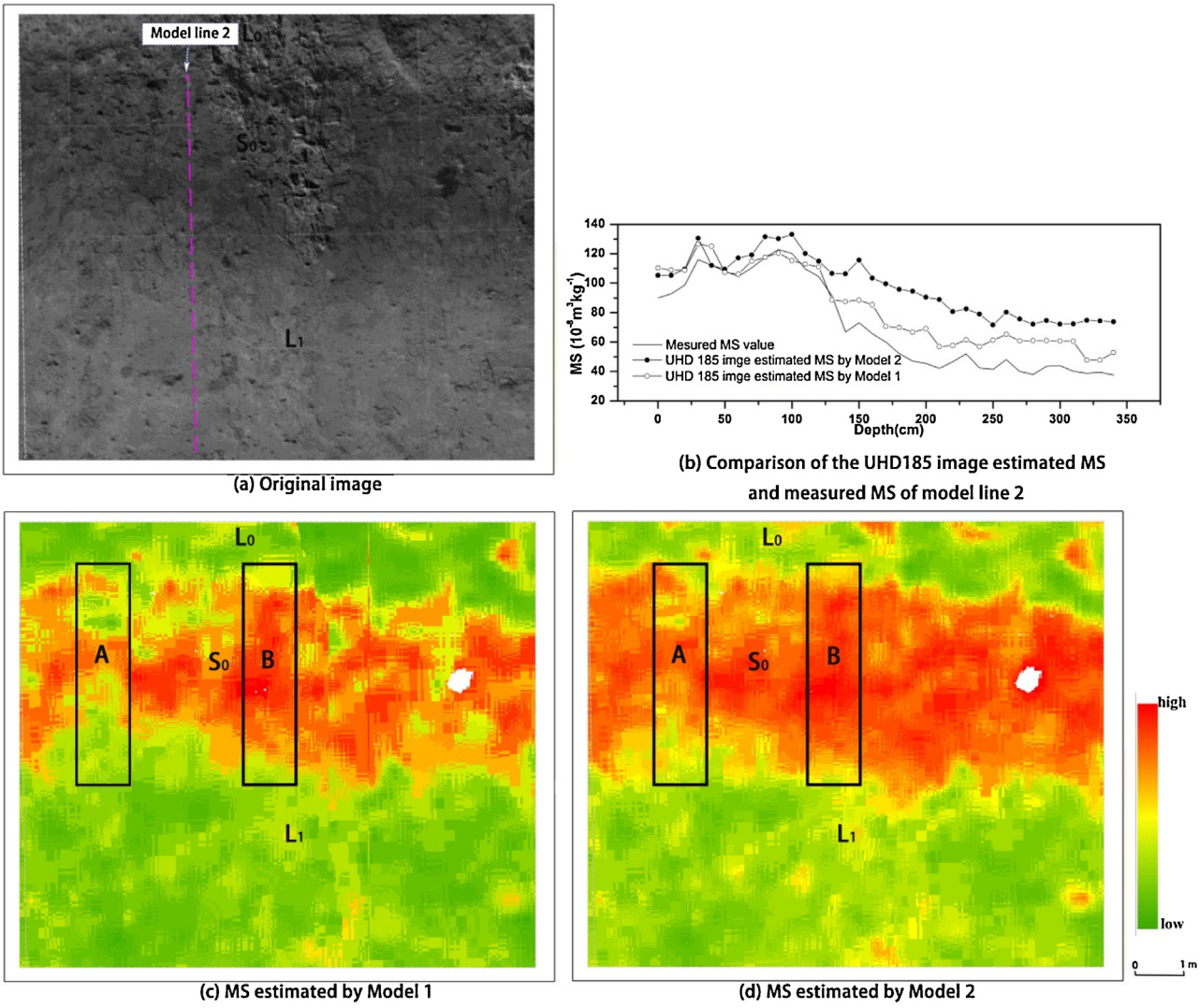

Fig. 10. MS estimates made with the regression models.(For interpretation of the references to colour in the text, the reader is referred to the web version of this article.)

UHD 185, a new generation of commercial hyperspectral imaging sensors, was used for the image acquisition. The accuracy of UHD 185 reflectance meets the requirements of MS estimation, except for the wavelength range of 900–950 nm. The MS values obtained from the UHD 185 data are convincing and consistent with the measured data. The estimated MS values from UHD 185 display excellent correlation coefficients (i.e., >0.85). The trend in changing MS values is clear, suggesting that models 1 and 2 could

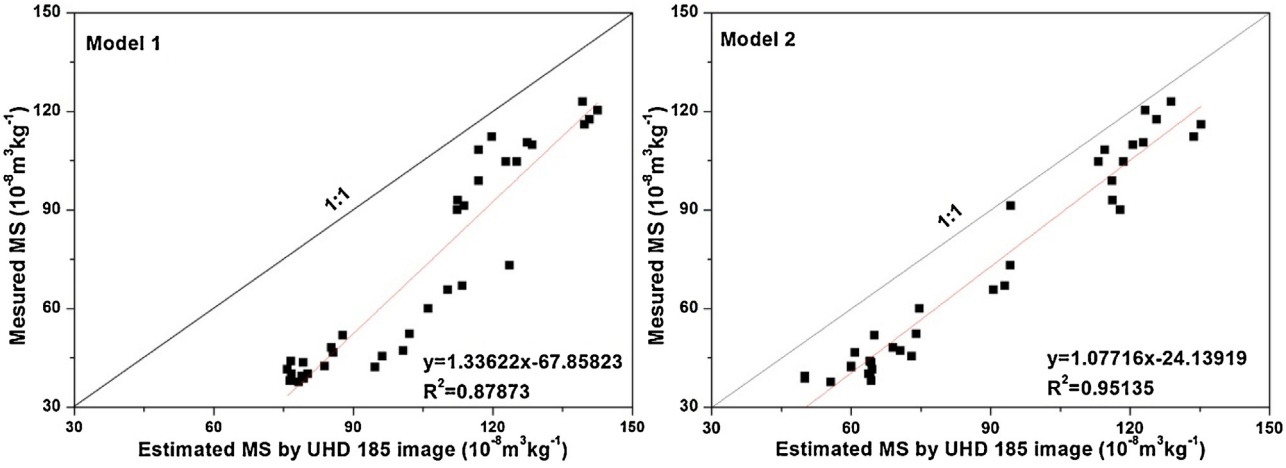

Fig. 11. Comparison plot of MS from laboratory measurements with MS estimated from the UHD 185 image by the VIS-NIR index.

produce reasonable loess-paleosol section surface maps from the UHD 185 image, although there is a linear offset between the estimated MS and the measured MS (Fig. 11). Because of the limit of the spectral range, the performances of models 3 and 4 were not discussed. However, they were demonstrated as successful according to laboratory test data.

The MS map derived from the UHD 185 corresponds well to the loess sequences. The MS map can overcome the limitation of a single (vertical) path to measure the MS, which sometimes represents site-specific influences rather than monsoonal changes (depending on the position of the path). The methodology proposed here can be used to map MS on a much larger scale.

Acknowledgments

This research was supported by grants from the National Natural Science Foundation of China (Grant No. 40972143 and 41374050), the Institute of Crustal Dynamics, China Earthquake Administration (Grant No. ZDJ2015-01) and the seismic hazard assessment of active fault in key area for earthquake surveillance of China (Grant No. 0115245). The authors wish to thank the anonymous reviewers for their constructive comments that helped improve the scholarly quality of the paper.

References

ViewSpec Pro™ User Manual, ASD Document 600555 Rev.A, Boulder, CO 80301.
An, Z.S., Kukla, G., Porter, S.C., Xiao, J.L., 1991. Magnetic susceptibility evidence of monsoon variation on the Loess Plateau of central China during the last 130,000 years. Quat. Res. 36, 29–36.
Bishop, J.L., Lane, M.D., Dyar, M.D., Brown, A.J., 1994. Reflectance and emission spectroscopy study of four groups of phyllosilicates: smectites, kaolinite–serpentines, chlorites and micas. Clay Miner. 43, 35–54.
Chen, J., Ji, J., Balsam, W., Chen, Y., Liu, L., An, Z., 2002. Characterization of the Chinese loess—paleosol stratigraphy by whiteness measurement. Palaeogeogr. Palaeoclimatol. Palaeoecol. 183, 287–297.
Clark, R.N., Roush, T.L., 1984. Reflectance spectroscopy: quantitative analysis techniques for remote sensing applications. J. Geophys. Res. 89, 6329–6340.
Clark, R.N., King, T.V.V., Klejwa, M., Swayze, G.A., Vergo, N., 1990. High spectral resolution reflectance spectroscopy of minerals. J. Geophys. Res. 95, 653–680.
Clark, R.N., 1999. Spectroscopy of the rocks and minerals, and principles of spectroscopy. In: Rencz, A.N. (Ed.), Remote sensing for Earth Sciences. Manual of Remote Sensing, vol. 3. John Wiley and Sons, New York, pp. 3–58.
Cui, J., Yan, B.K., Tian, F., Liu, D.C., Wang, R.S., Yang, S.M., Shen, W., 2014. Regional-scale minerals mapping using ASTER VNIR/SWIR data and validation of reflectance and mineral map products using airborne hyperspectral CASI/SASI data. Int. J. Appl. Earth Observ. Geoinform. 33, 127–141.
Deaton, B.C., Balsam, W.D., 1991. Visible spectroscopy—a rapid method for determining hematite and goethite concentration in geological materials. J. Sediment. Petrol. 61, 628–632.
Furundzic, D., 1998. Application example of neural networks for time series analysis: rainfall-runoff modeling. Signal Process 64 (3), 383–396.
Galva˜o, L.S., Pizarro, M.A., Epiphanio, J.C.N., 2001. Variations in reflectance of tropical soils: spectral-chemical composition relationships from AVIRIS data. Remote Sens. Environ. 75, 245–255.
Heller, F., Evans, M.E., 1995. Loess magnetism. Rev. Geophys. 33, 221–240.
Heller, F., Liu, T.S., 1982. Magnetostratigraphical dating of loess deposits in China. Nature 300, 431–432.
IBM SPSS, 2010. IBM SPSS Statistics Base 19. Chicago, IL :SPSS.
Ji, J., Balsam, W., Chen, J., 2001. Mineralogic and climatic interpretations of the Luochuan loess section (China) based on diffuse reflectance spectrophotometry. Quat. Res 56, 23–30.
Ji, J., Chen, J., Balsam, W., Lu, H., Sun, Y., Xu, H., 2004a. High resolution hematite/geothite records from Chinese loess sequences for the last glacial-interglacial cycle: rapid climatic response of the East Asian Monsoon to the tropical Pacific. Geophys. Res. Lett. 31, L03207.
Ji, J., Chen, J., Li, J., Zhang, W., Balsam, W., Lu, H., 2004b. Relating magnetic susceptibility (MS) to the simulated thematic mapper (TM) bands of the Chinese loess: application of TM image for soil MS mapping on Loess Plateau. J. Geophys. Res. 109, B05102.
Jin, L., Ji, J., William, B., Chen, J., Lu, H., 2003. Determinning magnetic susceptibility in loess-paleosol sections by near-infrared reflectance spectroscopy. Geophys. Res. Lett 30, 1–27.
Kohfeld, K.E., Harrison, S.P., 2003. Glacial-interglacial changes in dust deposition on the Chinese Loess Plateau. Quaternary Sci. Rev 22, 1859–1878.
Liu, T.S., 1985. Loess and the Environment. China Ocean Press, Beijing.
Maher, B.A., Hu, M.Y., Roberts, H.M., Wintle, A.G., 2003. Holocene loess accumulation and soil development at the western edge of the Chinese Loess Plateau: implications for magnetic prxiesl of palaeorainfall. Q. Sci. Rev. 22, 445–451.
Palacios- Orueta, A., Ustion, S.L., 1998. Remote sensing of soil properties in the Santa Monica Mountains I. Spectral analysis. Remote Sens. Environ. 65, 170–183.
Pokorny, J., Suza, P., Pokorny, P., Chlupacova, M., Hrouda, F., 2006. Widening power of low-field and high field magnetic methods in the investigation of rocks and environment materials using the Multi-function Kappabridge Set. Geophys. Res. Abstract 8, 04141.
Porter, S.C., Hallet, B., Wu, X., An, Z., 2001. Dependence of near-surface magnetic susceptibility on dust accumulation rate and precipitation on the Chinese Loess Plateau. Quat. Res. 55, 271–283.
Smith, M.J., Stevens, T., MacArthur, A., Malthus, T.J., Lu, H., 2011. Characterising Chinese loess stratigraphy and past monsoon variation using field spectroscopy. Q. Int. 234, 146–158.
Stevens, T., Lu, H., 2009. Optically simulated luminescence dating as a tool for calculating sedimentation rates in Chinese loess: comparisons with grain-size records. Sedimentology 56, 911–934.
Tompson, R., Oldfield, F., 1986. Environ. Magnetism. Allen & Unwin, London, pp. 227.
Verosub, K.L., Fine, P., Singer, M.J., TenPas, J., 1993. Pedogenesis and paleoclimate: interpretation of the magnetic susceptibility record of Chinese loess-paleosol sequences. Geology 21, 1011–1014.
Viscarra Rossel, R.A., Chen, C., 2011. Digitally mapping the information content of visible-near infrared reflectance spectra of surficial Australian soils. Eur. J. Soil Sci. Remote Sens. Environ. 115, 1443–1455.
Xu, X.W., Qiang, X.K., Fu, C.F., Zhao, H., Chen, T., Sun, Y.F., 2012. Characteristics of frequency-dependent magnetic susceptibility in Bartington MS2 and Kappabridge MFK1-FA, and its application in loess-paleosol, red clay and lacustrine sediments. Chin. J. Geophys. 55 (1), 197–206.
Zhi, H., Brian, J.T., Stephen, J.D., 2004. Estimating foliage nitrogen concentration from HYMAP data using continuum removal analysis. Remote Sens. Environ. 93 (10), 18–29.